*Sound & Vibration* 2026, 60(5), 4152.
doi: https://doi.org/10.59400/sv4152

Article

# Simulation and algorithmic implementation of ultrasonic phased-array imaging for curved lead-seal surfaces

**Jian Cheng***, **Liguang Hu**, **Fengyin Zhang**, **Quan Zhang**, **Lianbing Wang**

China Southern Power Grid Shenzhen Power Supply Bureau Co., Ltd., Shenzhen 518001, China

*** Corresponding author:** Jian Cheng, gdj8000@163.com

**CITATION**

Cheng J, Hu L, Zhang F, et al. Simulation and algorithmic implementation of ultrasonic phased-array imaging for curved lead-seal surfaces. Sound & Vibration. 2026; 60(5): 4152. https://doi.org/10.59400/sv4152

**ARTICLE INFO**

Received: 12 March 2026
Revised: 21 June 2026
Accepted: 8 July 2026
Available online: 27 July 2026



**Abstract:** In ultrasonic phased-array sector scanning of lead-seal defects in high-voltage cable terminations, incomplete contact between the probe and the curved lead-seal surface may cause acoustic-beam spreading, focal shift, weak defect echoes, image distortion, and near-surface artefacts. To address these problems, this study proposes a curvature-adaptive ultrasonic phased-array imaging method for curved lead-seal surfaces. First, an acoustic-field simulation model of the curved lead-seal structure was established to analyze beam propagation through the couplant layer and the lead seal. Then, a delay law based on Fermat's principle and Snell's law was derived to account for the curved interface and the two-layer propagation path. The calculated delays were applied during post-processing delay-and-sum beam synthesis, followed by Hilbert-envelope extraction and angular coordinate correction. Numerical results show that the curved interface causes beam spreading and focal-position shift compared with a flat interface, which explains the localization deviation in conventional phased-array imaging. Laboratory experiments were further conducted on lead-seal specimens with internal defects, interlayer defects, and combined internal–interlayer defects. For the internal defect with an actual depth of 15.0 mm, the positioning error was reduced from 13.33% to 6.67%. For the interlayer defect with an actual depth of 25.0 mm, the positioning error was reduced from 10.00% to 4.00%. The results demonstrate that the proposed method improves defect localization accuracy, morphology restoration, and imaging consistency compared with conventional phased-array imaging. This study provides a simulation-supported and experimentally validated method for curved lead-seal ultrasonic imaging, although further validation is still required for naturally formed irregular cracks, variable coupling conditions, and field cable-terminal applications.

**Keywords:** high-voltage cable termination; curved lead-seal surface; phased-array ultrasonic testing; delay-and-sum imaging; angular correction; defect localization

## 1. Introduction

High-voltage cables are critical components of urban power transmission systems, and their operational reliability is directly related to grid safety and power-supply stability. As an important sealing and connecting structure in high-voltage cable terminations, the lead seal provides sealing, waterproofing, grounding, and mechanical protection. However, under the combined effects of improper installation, material deformation, external mechanical loading, electrochemical corrosion, water ingress, and long-term service stress, lead-seal structures may develop defects such as voids, cracks, interlayer separation, and local deformation. Xu et al. investigated electrochemical corrosion and water-ingress defects in the lead-seal section of high-voltage cable intermediate joints and indicated that such defects can affect the insulation performance and sealing reliability of cable accessories [1]. Fang et al. studied phased-array ultrasonic testing and flexible-coupling inspection methods for lead-seal defects in high-voltage cable terminals, demonstrating the feasibility of ultrasonic testing for defect identification in this type of structure [2, 3]. Therefore, reliable nondestructive testing and quantitative imaging of lead-seal defects in high-voltage cable terminations are of significant engineering importance.

Ultrasonic phased-array testing has been widely applied in nondestructive testing owing to its beam-steering capability, electronic focusing capability, and intuitive imaging performance. Compared with conventional single-element ultrasonic testing, phased-array ultrasonic testing can realize sector-scan imaging or post-processed imaging through the coordinated excitation and reception of multiple array elements, thereby improving the efficiency of defect localization and characterization in complex structures. Drinkwater and Wilcox reviewed the application of ultrasonic arrays in nondestructive evaluation and highlighted their advantages in flexible inspection and rapid imaging [4]. Holmes et al. proposed a post-processing method based on the full matrix of ultrasonic transmit–receive array data, providing an important foundation for synthetic focusing and total-focusing-type imaging [5]. Zhang et al. further developed the multi-mode total focusing method, showing that post-processed imaging can effectively improve defect detection and characterization [6]. These studies indicate that ultrasonic phased-array testing and its post-processing imaging methods can enhance defect identification in complex structures, but imaging quality strongly depends on the accuracy of acoustic propagation modeling and delay-law calculation.

In practical engineering inspection, the tested objects often have curved surfaces or complex geometries. Surface curvature changes the acoustic-beam propagation path and may cause refraction, beam spreading, and focal-position shift, thereby affecting defect localization accuracy. Li et al. applied ultrasonic phased-array inspection to butt welds of complex-surface components and pointed out that surface geometry and beam-path determination are important factors influencing inspection results [7]. Cruza et al. proposed a high-speed hardware-based focal-law calculation method for automatic focusing, emphasizing the importance of efficient delay computation in phased-array imaging [8]. Miao et al. proposed an adaptive ultrasonic full-matrix-capture process for global imaging of complex components with curved surfaces, in which surface-profile information and propagation-path correction were incorporated into the imaging procedure [9]. Wang et al. developed a high-efficiency adaptive ultrasonic array imaging method for curved structures and improved imaging performance through sensitivity correction [10]. In addition, Chatillon et al. developed a flexible phased-array transducer for ultrasonic nondestructive testing of components with complex geometries [11], and Casula et al. further investigated smart flexible phased-array inspection for complex components [12]. For aeroengine casing ring forgings, where amplitude fluctuation and noise interference are significant, Guan et al. proposed an adaptive filtering and angle-gain compensation method for phased-array inspection [13]. These studies show that ultrasonic phased-array inspection of curved structures requires not only improved coupling conditions between the probe and the tested object, but also delay correction and imaging methods adapted to curved propagation paths.

In recent years, increasing attention has been paid to defect detection in high-voltage cable terminal lead seals. Peng et al. proposed an ultrasonic phased-array flexible-coupling method for defect detection in high-voltage cable terminal lead seals, and the results showed that flexible coupling can improve the contact condition between the probe and the curved lead-seal surface while also facilitating the identification of internal defects, interlayer defects, and combined internal–interlayer defects [14]. Zheng et al. proposed a quantitative ultrasonic testing method for lead-seal defects in high-voltage cable accessories, providing a reference for defect-size evaluation and localization analysis [15]. Fang et al. applied a one-dimensional phased array to three-dimensional imaging detection of lead-seal defects in high-voltage cable terminations, demonstrating the potential of volumetric characterization of lead-seal defects [16]. Zhou et al. introduced convolutional neural networks into ultrasonic image recognition of terminal lead-seal defects, indicating the potential of intelligent methods for interpreting lead-seal ultrasonic images [17]. These studies have laid an important foundation for ultrasonic testing of lead-seal defects. However, existing studies mainly focus on experimental inspection, flexible coupling, quantitative evaluation, three-dimensional reconstruction, or image recognition. The acoustic propagation changes caused by the curved lead-seal interface and their compensation mechanism in delay-and-sum imaging have not yet been systematically analyzed.

Beyond lead-seal inspection, recent studies on ultrasonic phased-array imaging have also moved toward intelligent interpretation, adaptive imaging, signal processing, and image enhancement. Tunukovic et al. evaluated the performance of machine-learning object detection in phased-array ultrasonic testing of carbon-fibre-reinforced plastics, showing that data-driven methods can be used for automatic defect identification [18]. Na et al. reviewed advances in machine learning for phased-array ultrasonic nondestructive testing and summarized its potential applications in imaging, defect recognition, and data processing [19]. Ma et al. combined ultrasonic phased-array testing with convolutional neural networks to identify multiple types of internal defects in carbon-fibre-reinforced plastics [20]. Nicolson et al. investigated an in-process ultrasonic phased-array inspection method for narrow-gap welds and indicated that adaptive imaging and delay strategies are important for inspection reliability under complex conditions [21]. Chen et al. proposed a denoising method for ultrasonic weld-defect signals, showing that appropriate signal processing can improve the stability of defect interpretation [22]. Deng et al. studied an ultrasonic phased-array inspection method for crack defects in butt joints of multilayered steel vessels for high-pressure hydrogen storage, verifying the applicability of phased-array testing to complex engineering structures [23]. Pan et al. investigated total-focusing imaging based on phase coherence and dB amplitude enhancement, showing that coherent information and amplitude enhancement can improve defect imaging [24]. Zhu et al. proposed an ultrasonic nondestructive testing image-enhancement model based on super-resolution imaging, further indicating the importance of image enhancement for quantitative defect evaluation [25]. These studies suggest that propagation modeling, delay correction, signal processing,and quantitative image evaluation are important technical routes for improving the performance of ultrasonic phased-array testing in complex structures.

However, several problems remain for curved lead-seal structures in high-voltage cable terminations. First, the curvature of the lead-seal surface and the couplant layer cause refraction and changes in the acoustic propagation path at the couplant–lead interface, while the conventional planar-interface delay model cannot accurately describe the actual two-layer propagation process. Second, although phased-array inspection of curved components, flexible coupling, adaptive full-matrix imaging, and intelligent recognition methods have been reported, the relationship among curved-interface acoustic-field simulation, delay-law calculation, echo-signal alignment, and final image reconstruction remains insufficiently clarified for curved lead-seal structures. Third, existing studies on lead-seal defect detection mainly rely on image comparison and qualitative analysis, while quantitative localization errors for defects at different depths and of different types still require further investigation. Therefore, it is necessary to establish a curvature-adaptive delay model for curved lead-seal structures and verify its effectiveness through both acoustic-field simulation and experiments using specimens with known defects.

To address these issues, this study proposes a curvature-adaptive ultrasonic phased-array imaging method for defect detection in curved lead seals of high-voltage cable terminations. The main contribution of this study lies in the integration of curved-interface delay calculation, delay-and-sum beam synthesis, Hilbert-envelope extraction, angular coordinate correction, and experimental validation for lead-seal defects, rather than the simple application of general ray-tracing methods. First, a curved couplant–lead interface propagation model is established based on Fermat's principle and Snell's law to calculate the incidence point and propagation time from different array elements to the imaging point. Second, an acoustic-field simulation model is established to compare the beam-propagation characteristics under flat-interface and curved-interface conditions, thereby clarifying beam spreading and focal-position shift induced by surface curvature. Third, the calculated delay is converted into sampling-point compensation and applied to post-processing delay-and-sum imaging, while Hilbert-envelope extraction and angular coordinate correction are combined to obtain the lead-seal defect image. Finally, experiments are conducted on lead-seal specimens containing internal defects, interlayer defects, and combined internal–interlayer defects, and the results are quantitatively compared with those obtained using conventional phased-array imaging.

## 2. Curvature-adaptive delay calculation for phased-array ultrasonic imaging of curved lead-seal surfaces

In phased-array ultrasonic testing of curved lead-seal surfaces, the curved geometry of the lead seal and the existence of the couplant layer significantly affect ultrasonic wave propagation. When the ultrasonic beam emitted from a phased-array transducer reaches the couplant-lead interface, refraction occurs because the sound velocity in the couplant differs from that in the lead seal. Therefore, the conventional geometric path-difference method, which is usually suitable for planar or single-layer media, may introduce delay errors when it is directly applied to curved lead-seal structures. These delay errors may further lead to focal shift, weak defect indication, and defect-location deviation in ultrasonic imaging.

To address this problem, a curvature-adaptive delay calculation method based on Fermat's principle and Snell's law is adopted in this study. According to Fermat's principle, ultrasonic waves propagate along the path that requires the minimum travel time in multilayer media. Therefore, before calculating the propagation time from each array element to a given focal point, the incidence point on the curved couplant-lead interface must be determined first. The geometric model used for the delay calculation is shown in **Figure 1**.

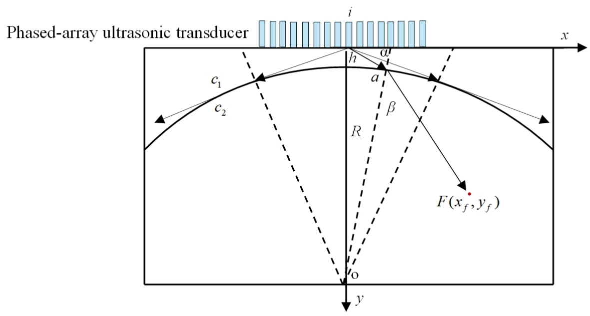


**Figure 1.** Schematic diagram of ultrasonic beam path calculation for lead-sealed surface.

A Cartesian coordinate system is established with the centre of the phased-array transducer as the origin. The horizontal direction along the array is defined as the positive *x*-axis, and the vertical downward direction is defined as the positive *y*-axis. The curved lead-seal interface is approximated as a circular arc, and its equation can be expressed as

$$x^2 + (y - h - R)^2 = R^2, \quad y \leq h + R \tag{1}$$

where *R* is the curvature radius of the lead-seal surface, *h* is the thickness of the liquid couplant along the central axis, and O(0, *h* + *R*) is the centre of curvature of the curved lead-seal interface.

For the *i*-th array element $E_i(x_i,0)$, the acoustic beam first travels through the couplant and reaches the curved interface at the incidence point $a(m,n)$. It then refracts into the lead seal and propagates to the focal point $F(x_f,y_f)$. To describe this propagation path clearly, three vectors are introduced.

The normal-direction vector from the incidence point a to the centre of curvature O is defined as

$$r_a = (-m, h + R - n) \tag{2}$$

where $r_a$ denotes the normal-direction vector of the curved interface at the incidence point $a(m,n)$. Since a lies on the circular interface, the magnitude of $r_a$ is equal to the curvature radius *R*.

The incident acoustic-ray vector from the incidence point $a(m,n)$ to the *i*-th array element $E_i(x_i,0)$ is defined as

$$s_{1i} = (x_i - m, -n) \tag{3}$$

where $s_{1i}$ denotes the incident acoustic-ray vector in the couplant corresponding to the $i$-th array element.

The refracted acoustic-ray vector from the incidence point $a(m,n)$ to the focal point $F(x_f,y_f)$ is defined as

$$s_2 = (x_f - m, y_f - n) \tag{4}$$

where $s_2$ denotes the refracted acoustic-ray vector inside the lead seal.

The incidence angle α is defined as the angle between the normal-direction vector $r_a$ and the incident acoustic-ray vector $s_{1i}$. According to the cross-product relationship, one obtains

$$|r_a \times s_{1i}| = |r_a||s_{1i}| \sin\alpha \tag{5}$$

where $\alpha$ is the incidence angle in the couplant. Substituting Equations (2) and (3) into Equation (5), and considering $|r_a| = R$, gives

$$\sin\alpha = \frac{mn - (x_i - m)(h + R - n)}{R\sqrt{(x_i - m)^2 + n^2}} \tag{6}$$

where $x_i$ is the horizontal coordinate of the $i$-th array element, and $m$ and $n$ are the coordinates of the incidence point on the curved lead-seal interface.

Similarly, the refraction angle $\beta$ is defined as the angle between the normal-direction vector $r_a$ and the refracted acoustic-ray vector $s_2$. According to the cross-product relationship, one obtains

$$|r_a \times s_2| = |r_a||s_2| \sin\beta \tag{7}$$

where $\beta$ is the refraction angle inside the lead seal. Substituting Equations (2) and (4) into Equation (7) gives

$$\sin\beta = \frac{-m(y_f - n) - (x_f - m)(h + R - n)}{R\sqrt{(x_f - m)^2 + (y_f - n)^2}} \tag{8}$$

where $x_f$ and $y_f$ are the coordinates of the focal point $F$ inside the lead seal.

The incidence angle $\alpha$ and refraction angle $\beta$ satisfy Snell's law:

$$\frac{\sin\alpha}{c_1} = \frac{\sin\beta}{c_2} \tag{9}$$

where $c_1$ is the sound velocity in the couplant, and $c_2$ is the sound velocity in the lead seal. In this study, $c_1 < c_2$.

By substituting Equations (6) and (8) into Equation (9), and combining the result with the curved-interface equation in Equation (1), the incidence point $a(m,n)$ can be solved from the following nonlinear equation system:

$$\begin{cases} \dfrac{mn - (x_i - m)(h + R - n)}{c_1 R\sqrt{(x_i - m)^2 + n^2}} = \dfrac{-m(y_f - n) - (x_f - m)(h + R - n)}{c_2 R\sqrt{(x_f - m)^2 + (y_f - n)^2}} \\ m^2 + (n - h - R)^2 = R^2, n \le h + R \end{cases} \tag{10}$$

where the first equation is derived from Snell's law, and the second equation constrains the incidence point *a*(*m*,*n*) to lie on the curved lead-seal interface. The unknowns in Equation (10) are *m* and *n*. Once these two unknowns are solved, the actual acoustic propagation path from the array element to the focal point can be determined.

It should be noted that the numerator on the right-hand side of the first equation in Equation (10) is

$$-m\left(y_f-n\right)-\left(x_f-m\right)\left(h+R-n\right)$$

which is obtained from the expansion of the cross product $r_\mathrm{a} \times s_2$. Therefore, this term contains two subtractive terms rather than a triple-product term. This correction avoids the dimensional inconsistency in the original expression and ensures the reliability of the subsequent delay calculation.

After solving Equation (10), the coordinates of the incidence point *a*(*m*,*n*) can be obtained. The acoustic path length in the couplant is calculated as

$$l_1=\sqrt{\left(m-x_i\right)^2+n^2} \tag{11}$$

where $l_1$ is the acoustic path length from the *i*-th array element $E_i$ to the incidence point a in the couplant. The corresponding propagation time in the couplant is

$$T_1=\frac{l_1}{c_1} \tag{12}$$

where $T_1$ is the propagation time in the couplant.

The acoustic path length inside the lead seal is calculated as

$$l_2=\sqrt{\left(x_f-m\right)^2+\left(y_f-n\right)^2} \tag{13}$$

where $l_2$ is the acoustic path length from the incidence point $a$ to the focal point $F$ inside the lead seal. The corresponding propagation time inside the lead seal is

$$T_2=\frac{l_2}{c_2} \tag{14}$$

where $T_2$ is the propagation time inside the lead seal.

Thus, the total propagation time from the $i$-th array element to the focal point $F$ is

$$T_{iF}=T_1+T_2 \tag{15}$$

where $T_{iF}$ is the total propagation time from the $i$-th array element to the focal point $F$.

Repeating the above calculation for all $N$ array elements gives the propagation-time set

$$T_F=\{T_{1F},T_{2F},\ldots,T_{NF}\} \tag{16}$$

where $T_F$ denotes the set of propagation times from all array elements to the same focal point $F$, and $N$ is the total number of array elements.

The delay time for the $i$-th array element is then calculated as

$$\Delta T_i = \max\left(T_F\right) - T_{iF} \tag{17}$$

where $\Delta T_i$ is the delay time applied to the $i-$th array element, and $\max(T_F)$ represents the maximum propagation time among all array elements. By using Equation (17), the echo signals received by different array elements can be aligned in phase before coherent summation.

Using the above procedure, the delay times required for all array elements to focus at a given point inside the lead seal can be obtained. By substituting different focal-point coordinates into Equation (10), the delay laws for different imaging points or scan lines can be calculated.

In this study, the transient acoustic simulation is used to acquire the echo signals received by the array elements under different steering angles. The curvature-adaptive delay law derived above is then applied during the post-processing stage. Specifically, the calculated delay time $\Delta T_i$ is converted into the corresponding number of sampling points and used to align the received echo signals from different elements before delay-and-sum beam synthesis. In this way, the proposed delay calculation directly determines the phase alignment of the received signals and improves the focusing accuracy for ultrasonic imaging of curved lead-seal defects.

## 3. Simulation study of acoustic field characteristics for ultrasonic phased array on lead sealing curved surface

### 3.1. Numerical model and simulation settings

To investigate the influence of the curved lead-seal surface on ultrasonic wave propagation and to obtain the defect echo signals required for subsequent imaging, a two-dimensional ultrasonic phased-array simulation model of the curved lead-seal structure was established. The model consisted of the phased-array transducer, the liquid couplant layer, the curved lead seal, an artificial defect, and the aluminum sheath. The geometric model is shown in **Figure 2**.

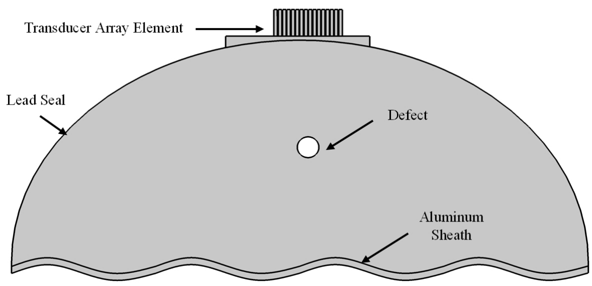


**Figure 2.** Simulation model of the lead sealing curved surface for the high voltage (HV) cable termination.

In the simulation model, the curved lead-seal surface was simplified as a convex circular interface. The liquid couplant was placed between the phased-array transducer and the lead-seal surface. The artificial defect was set as a circular hole inside the lead seal. The centre of the circular defect was located on the central axis of the array, 15 mm below the upper surface of the lead seal, and the defect diameter was 3 mm. The couplant thickness was set to 2 mm.

The sector-scan range of the phased-array probe was set from −30° to 30°, with an angular step of 1°. At each steering angle, the echo signals reflected from the defect were received by 16 array elements. The 16-element configuration was selected to be consistent with the phased-array probe used in the subsequent experimental verification, rather than being an arbitrary numerical setting.

To improve the reproducibility of the simulation, the main numerical parameters and boundary conditions are summarized in **Table 1**.

**Table 1.** Numerical model parameters and simulation settings.

| Parameter | Setting |
|---|---|
| Simulation type | Two-dimensional pressure-acoustics transient simulation |
| Couplant thickness | 2 mm |
| Couplant sound velocity | 1,540 m/s |
| Lead sound velocity | 2,300 m/s |
| Defect type | Circular hole |
| Defect diameter | 3 mm |
| Defect depth | 15 mm below the upper lead-seal surface |
| Centre frequency | 2 MHz |
| Number of array elements | 16 |
| Steering range | −30°–30° |
| Steering step | 1° |
| Time step | 0.0125 μs |
| Total transient time | 14 μs |
| Solver | Pressure Acoustics, Transient |
| Defect boundary | Rigid acoustic boundary |

The circular defect and the aluminum sheath were set as rigid acoustic boundaries to obtain distinct reflected echo signals. The side boundaries of the model were set as pressure-release boundaries to reduce unwanted reflected waves from the lateral sides. Compared with the expressions “hard sound-field boundary” and “soft sound-field boundary” used in the original manuscript, the terms “rigid acoustic boundary” and “pressure-release boundary” are more standard in acoustic simulation.

The transient simulation was used to acquire the time-domain echo signals received by each array element under different steering angles. These simulated echo signals were then used as the input data for the delay-and-sum imaging algorithm described in Section 4.

### 3.2. Frequency-domain acoustic-field analysis of flat and curved interfaces

Before acquiring the time-domain defect echo signals, the acoustic-field characteristics of phased-array ultrasound passing through different interface geometries were analyzed. The purpose of this analysis was to explain why the curved lead-seal surface may cause focal shift, beam spreading, and defect-location deviation in conventional phased-array imaging.

For comparison, two interface models were considered. In the first model, the lead-seal interface was set as a flat interface. In the second model, the lead-seal interface was set as a convex curved interface. The centre frequency of the transducer was 2 MHz. The first medium was the liquid couplant, and the second medium was the lead seal. The thickness of the couplant layer was 2 mm, and the lead-seal region had a depth of 40 mm. The widths of the two media were both set to 14 mm.

As shown in **Figure 3**, when the ultrasonic beam passes through the flat interface, the acoustic energy remains relatively concentrated after entering the lead seal, and the beam width becomes narrower near the focal region. The main focal region appears at approximately 5 mm below the interface.

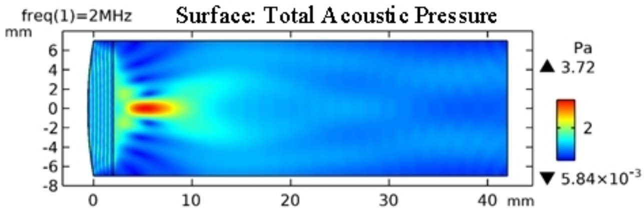


**Figure 3.** Two-dimensional sound field distribution of sound beams passing through the lead sealing flat interface.

In contrast, as shown in **Figure 4**, when the ultrasonic beam passes through the convex curved interface, the beam becomes wider and the focal region shifts deeper into the lead seal. The main focal region appears at approximately 10 mm below the interface. Compared with the flat-interface case, the curved-interface case shows more obvious beam spreading and focal-position shift.

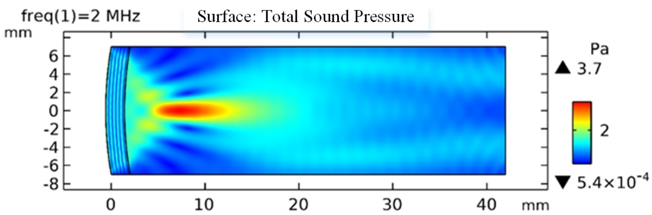


**Figure 4.** Two-dimensional sound field distribution of sound beams passing through the lead sealing convex interface.

This result indicates that the curved lead-seal surface changes the actual propagation path of the ultrasonic beam. If a conventional planar-interface delay law is directly used for curved lead-seal imaging, the calculated focal position may deviate from the actual acoustic focal position. This is one of the main reasons for defect-location deviation and morphology distortion in conventional phased-array imaging of curved lead-seal defects.

**Figure 5** further compares the sound-pressure distribution along the central axis. The difference between the flat and curved interfaces confirms that the curved geometry affects both acoustic-energy concentration and focal-depth position. Therefore, the curvature-adaptive delay calculation described in Section 2 is necessary for improving the focusing accuracy of curved lead-seal ultrasonic imaging.

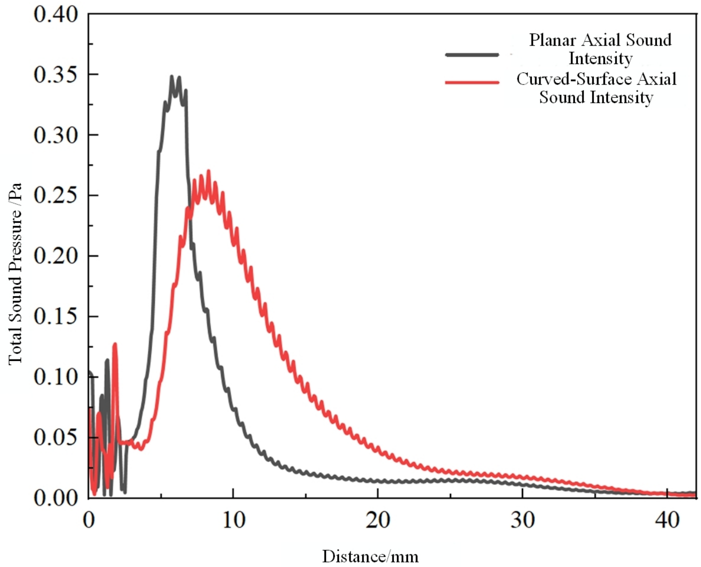


**Figure 5.** Sound pressure distribution along the central axis of the aluminum sealing.

## 3.3. Time-domain defect-echo acquisition

After analyzing the acoustic-field characteristics, a transient simulation was conducted to acquire the time-domain echo signals from the artificial circular defect in the curved lead seal. The defect was located 15 mm below the upper surface of the lead seal, and its diameter was 3 mm. The phased-array probe performed sector scanning from −30° to 30° with a step of 1°. At each steering angle, the echo signals received by the 16 array elements were recorded.

**Figure 6** shows the defect echo signals received by the 16 array elements when the steering angle is 0°. The acoustic wave reflected from the couplant layer is mainly submerged in the initial pulse region. The defect echo signals received by different elements show different amplitudes and phases because the propagation paths from the defect to the individual elements are different. The single-element defect echo amplitude is relatively weak, with an amplitude range of approximately −2–2 Pa.

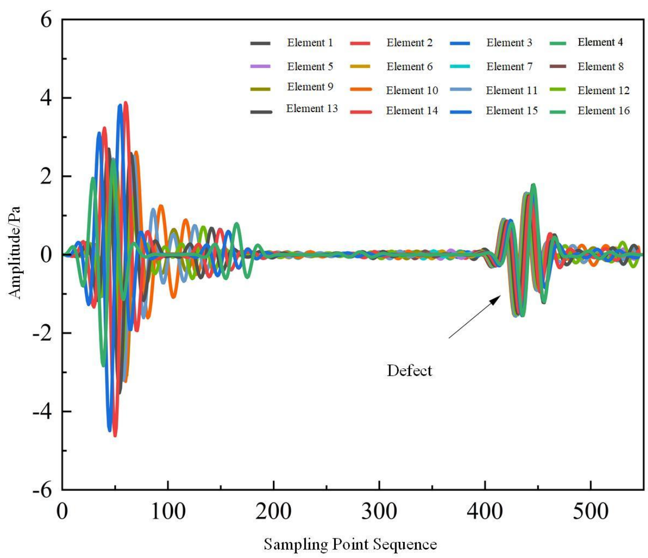


**Figure 6.** Echo signals from a lead sealing defect received by elements 1–16 at 0° steering angle.

The weak single-element echo amplitude is reasonable. First, the signal experiences two-way propagation attenuation during transmission and reception. Second, the curved lead-seal interface causes beam spreading and reduces the acoustic energy concentrated at the defect. Third, the 3-mm circular defect has a limited scattering cross-section. Finally, the initial pulse and couplant-layer reflection may interfere with the early part of the received signal. Therefore, the single-element echo amplitude should not be directly compared with the incident sound-pressure amplitude obtained from the frequency-domain acoustic-field distribution.

**Figure 7** shows the defect echo signals received by the 16 array elements when the steering angle is 15°. Compared with the 0° steering case, the defect echo amplitudes are lower. This is because, at 0°, the acoustic beam is directed closer to the defect position and the defect echo can be more effectively received by the array elements. However, at 15°, the acoustic beam deviates from the defect position, resulting in weaker defect echoes.

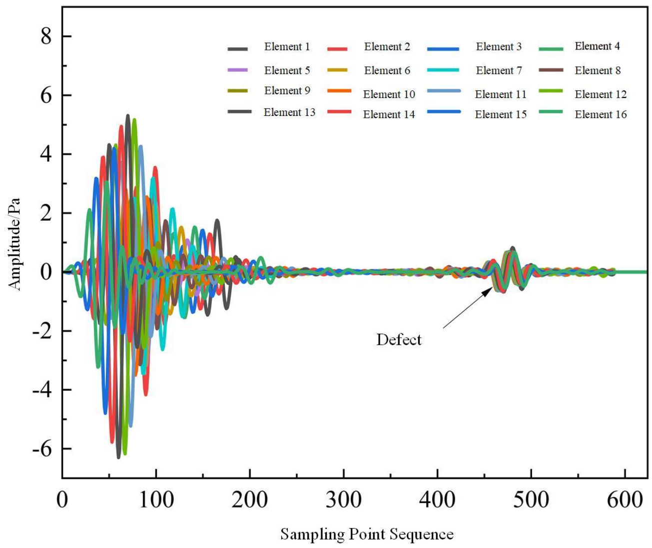


**Figure 7.** Echo signals from a lead sealing defect received by elements 1–16 at 15° steering angle.

The time-domain echo signals obtained in this section provide the basic data for the imaging algorithm in Section 4. In the subsequent delay-and-sum processing, the curvature-adaptive delay law derived in Section 2 is used to align the echo signals received by different elements. After phase alignment and coherent summation, the defect echo can be enhanced, which improves the imaging quality of curved lead-seal defects.

## 4. Curvature-adaptive imaging algorithm for curved lead-seal defects

After obtaining the time-domain defect echo signals from the numerical simulation, a curvature-adaptive imaging algorithm was used to reconstruct the ultrasonic image of the curved lead-seal defect. The purpose of this algorithm is to compensate for the propagation-time difference caused by the curved couplant–lead interface and to improve the phase consistency of the echo signals received by different array elements.

The imaging process mainly includes three steps. First, the time delays calculated from the curved-surface propagation model are converted into corresponding sampling-point shifts. Second, the echo signals received by different array elements are aligned and summed to synthesize the defect echo signal. Third, the synthesized signal is processed by Hilbert envelope extraction and angular coordinate correction to obtain the final ultrasonic image of the curved lead-seal defect.

### 4.1. Delay-and-sum processing of lead-seal defect echo signals

During delay-and-sum processing, the echo signal received by each array element must be shifted according to its propagation time. Since the echo data are stored as discrete sampling sequences, the time delay can be converted into an equivalent number of sampling points. Therefore, the delay adjustment of the echo signal is implemented by adding or removing a corresponding number of sampling points from the sampled data sequence.

For the $i$-th array element, the number of sampling points used for delay compensation can be calculated as

$$n_i = \Delta t_i f \tag{18}$$

where $n_i$ is the number of sampling points required for delay adjustment of the $i$-th array element, $\Delta t_i$ is the delay time corresponding to the $i$-th array element, and $f$ is the sampling frequency.

In practical processing, the echo signals received by different elements are delayed separately. For a given steering angle, the element closer to the focal point has a shorter propagation path and requires a smaller delay compensation. Conversely, the element farther from the focal point has a longer propagation path and requires a larger delay compensation. After delay adjustment, the sampling sequences of all elements are kept at the same length to ensure that the echo signals can be aligned in phase before summation.

**Figure 8** shows the number of sampling points required for delay adjustment under five representative sector-scan steering angles, namely, $-30°$, $-15°$, $0°$, $15°$, and $30°$.

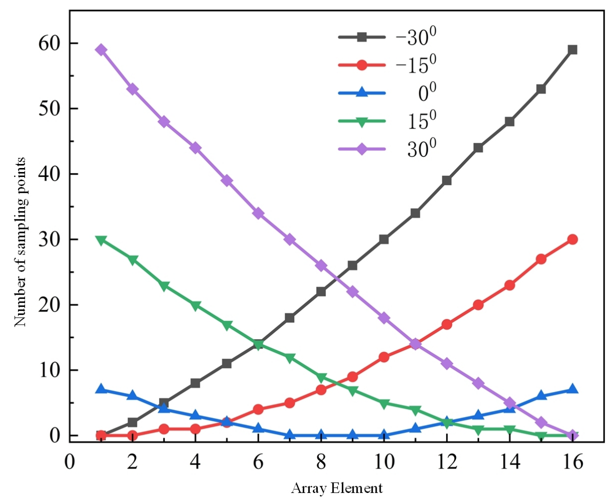


**Figure 8.** Number of sampling points for delay adjustment of 5 scan lines.

As shown in **Figure 8**, the delay compensation varies with both the array element number and the steering angle. For the $-30°$ scan line, element 1 requires the smallest delay compensation, while element 16 requires the largest delay compensation. For the $30°$ scan line, the trend is approximately reversed. This indicates that the required delay compensation changes with the beam steering direction.

For the $0°$ scan line, the delay distribution is approximately symmetric with respect to the centre of the array. This is consistent with the fact that the acoustic paths from the left and right elements to the central focal direction are nearly symmetric. In contrast, for oblique scan lines, such as $-15°$, $15°$, $-30°$, and $30°$, the delay distributions become asymmetric. This result confirms that a fixed delay rule cannot be used for all scan lines. Instead, the delay compensation must be calculated separately for each steering angle and each array element.

After the delay compensation is applied to the echo signals received by all 16 elements, the aligned signals are summed to obtain the synthesized defect echo signal. The synthesized beam signals at $0°$ and $15°$ steering angles are shown in **Figure 9**.

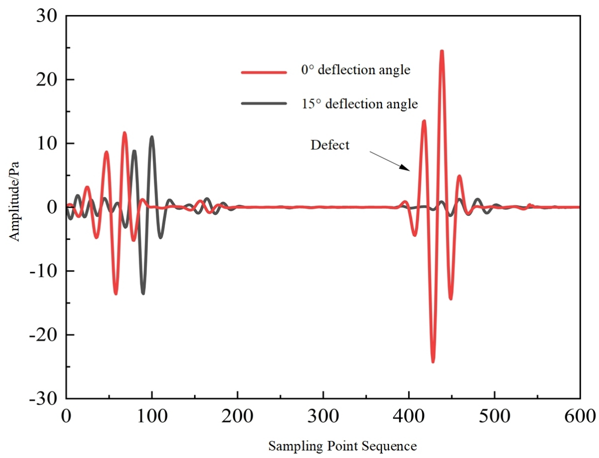


**Figure 9.** Combined beam signals of lead seal defect echoes at 0° and 15° deflection angles.

As shown in **Figure 9**, the synthesized beam signal at $0°$ has a significantly higher amplitude than the individual element echo signal. This indicates that the delay-and-sum process can enhance the coherent defect echo after phase alignment. In contrast, the synthesized beam signal at $15°$ has a lower amplitude, and the defect echo is not obvious. This is because the $15°$ beam direction deviates from the defect position, resulting in weaker reflected energy from the defect. Therefore, the synthesized beam amplitude can reflect the relationship between the steering direction and the defect location.

## 4.2. Hilbert envelope extraction of the synthesized signal

After delay-and-sum processing, the synthesized ultrasonic signal still contains high-frequency oscillations caused by the carrier wave. Directly using the oscillating signal for imaging may lead to discontinuous grayscale distribution and unclear defect boundaries. Therefore, Hilbert transform is used to extract the envelope of the synthesized defect echo signal.

Let $x(t)$ represent the synthesized ultrasonic signal of the lead-seal defect. The

Hilbert transform of $x(t)$ is expressed as

$$h(t) = \frac{1}{\pi}\int_{-\infty}^{+\infty}\frac{x(\tau)}{t - \tau}d\tau \tag{19}$$

where $h(t)$ is the Hilbert transform of $x(t)$, $t$is the observation time, and $\tau$ is the integration variable.

The analytic signal corresponding to $x(t)$can be written as

$$z(t) = x(t) + jh(t) \tag{20}$$

where $z(t)$ is the analytic signal, and $j$ is the imaginary unit.

The envelope amplitude of the synthesized ultrasonic signal is then obtained as

$$A(t) = \sqrt{x^2(t) + h^2(t)} \tag{21}$$

where $A(t)$ is the envelope amplitude of the synthesized signal.

**Figure 10** shows the synthesized signal before and after Hilbert envelope extraction.

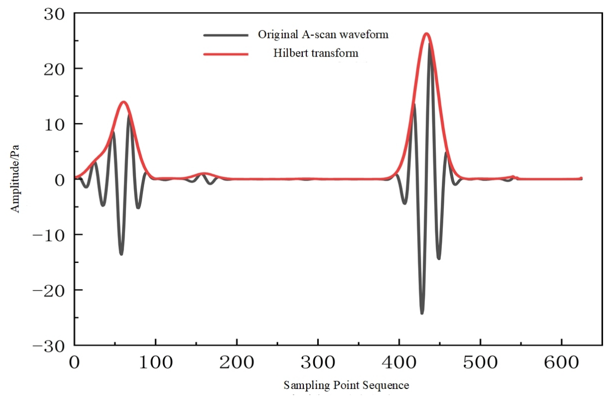


**Figure 10.** Combined beam signals of lead seal defect echoes.

In **Figure 10**, the black curve represents the synthesized signal after delay-and-sum processing, while the red curve represents the envelope extracted by Hilbert transform. Compared with the original synthesized signal, the envelope curve is smoother and can better describe the amplitude variation of the defect echo. It should be noted that the Hilbert transform is used here for envelope extraction and signal display, rather than as an independent denoising method. Its main function is to obtain a smoother amplitude representation of the synthesized echo signal, making the defect feature easier to observe in subsequent imaging.

After envelope extraction, the synthesized beam signals under different steering angles are arranged to form a B-scan image, as shown in **Figure 11**.

In **Figure 11**, the horizontal coordinate represents the scanning angle from $-30°$to $30°$, with a scanning step of $1°$. Therefore, a total of 61 scanning angles are included. The vertical coordinate represents the number of sampling points. It can be observed that one defect indication appears within the sampling-depth range of approximately 400–500 sampling points. However, the B-scan image is still displayed in the angle–sampling-point coordinate system. This coordinate system cannot directly reflect the actual spatial position of the defect inside the lead seal. In addition, the defect shape in the B-scan image is distorted to some extent. Therefore, angular coordinate correction is required to transform the B-scan data into the actual imaging coordinate system of the curved lead seal.

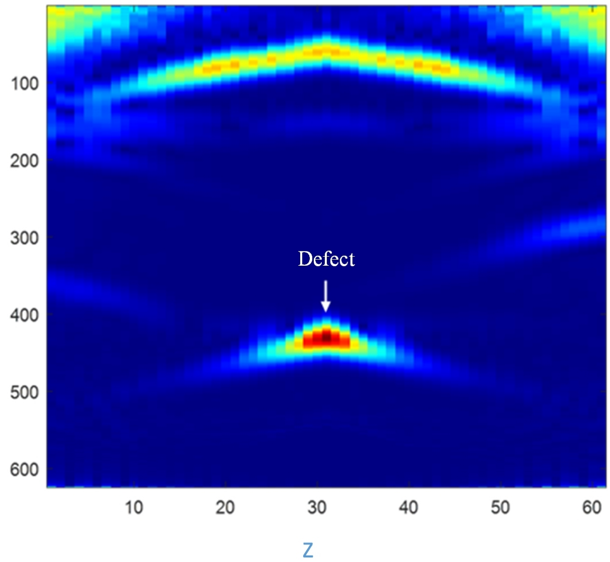


**Figure 11.** Lead seal defect B-scan imaging.

### 4.3. Angular coordinate correction for B-scan imaging

After Hilbert envelope extraction, the lead-seal defect echo data are stored in a B-scan image matrix. To obtain the actual ultrasonic image of the curved lead-seal region, the B-scan matrix needs to be transformed from the angle–sampling-point coordinate system into a spatial coordinate system.

The principle of angular coordinate correction is shown in **Figures 12–13**.

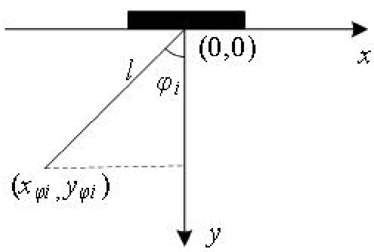


**Figure 12.** Transducer center coordinates.

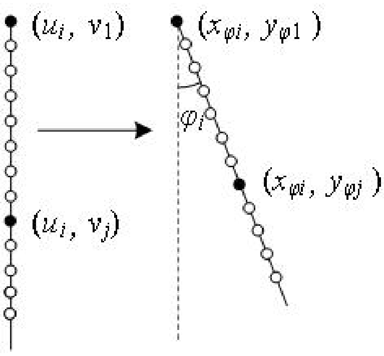


**Figure 13.** Coordinate mapping diagram.

As shown in **Figure 12**, the centre element of the phased-array transducer is defined as the coordinate origin $(0, 0)$. A scan line is emitted from this origin, and the angle between the scan line and the positive $y$-axis is defined as the steering angle $\phi_i$. The synthesized echo signal corresponding to each scan line has the same sequence length after delay compensation.

In the B-scan image matrix, the data point located at the $j$-th sampling point of the $i$-th scan line corresponds to a steering angle $\phi_i$. The steering angle of the $i$-th scan line can be expressed as

$$\phi_i = \theta_a + (i - 1)\Delta\theta \tag{22}$$

where $\phi_i$ is the steering angle of the $i$-th scan line, $\theta_a$ is the starting scanning angle, and $\Delta\theta$ is the angular scanning step. In this study, the scanning angle ranges from $-30°$to $30°$, and the angular step is $1°$.

For the $j$-th sampling point on the $i$-th scan line, the coordinate transformation can be written as

$$x_{\phi i} = v_j \sin\phi_i \tag{23}$$

$$y_{\phi i} = v_j \cos\phi_i \tag{24}$$

where $v_j$ represents the sampling-point position along the scan line, and $(x_{\phi i}, y_{\phi i})$ represents the mapped spatial coordinate after angular correction.

Through this transformation, the original B-scan data in the angle–sampling-point coordinate system are converted into spatial coordinate data. After matrix assignment, interpolation, and image filling, the corrected ultrasonic image of the curved lead-seal defect can be obtained.

### 4.4. Curved lead-seal imaging result and comparison with conventional phased-array imaging

After angular coordinate correction, the ultrasonic imaging result obtained by the proposed curved lead-seal imaging algorithm is shown in **Figure 14**.

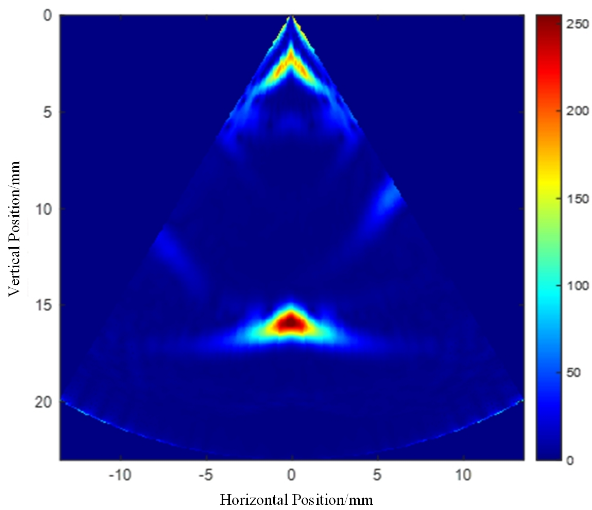


**Figure 14.** Lead seal curved surface ultrasonic phased array imaging.

As shown in **Figure 14**, the defect reconstructed by the proposed curved-surface imaging algorithm is mainly distributed at a depth of approximately 15–17 mm, with a lateral width of approximately −2–2 mm. This result is close to the simulated defect position, indicating that the proposed algorithm can effectively compensate for the influence of the curved lead-seal surface and reduce defect-position deviation.

For comparison, the imaging result obtained by the conventional phased-array imaging algorithm is shown in **Figure 15**.

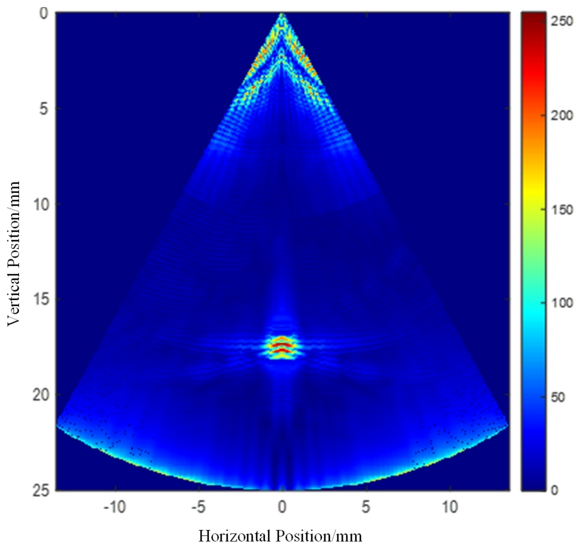


**Figure 15.** Ultrasonic phased array imaging.

As shown in **Figure 15**, the defect reconstructed by the conventional phased-array imaging algorithm appears at a deeper position, approximately 18–19 mm. In addition, the reconstructed defect width is narrower than that obtained by the proposed curved-surface imaging algorithm. This indicates that the conventional algorithm is affected by the curved interface and cannot accurately describe the actual defect position and morphology.

Using the defect centre as the reference point, the positioning error of the proposed curved lead-seal imaging algorithm is calculated to be 5.88%, while that of the conventional phased-array imaging algorithm is 8.82%. This comparison shows that the proposed algorithm provides better localization accuracy than the conventional method.

The comparison between **Figures 14–15** further indicates that the conventional phased-array imaging result has an elliptical defect shape and a weaker defect indication. In contrast, the proposed curved-surface imaging algorithm produces a clearer defect feature, higher image amplitude, and a reconstructed morphology that is closer to the simulated defect geometry.

To further compare the signal enhancement effect of the two imaging algorithms, the defect echo synthetic beam signals are shown in **Figure 16**.

In **Figure 16**, the black curve represents the defect synthetic beam signal obtained by the conventional ultrasonic phased-array imaging algorithm, while the red curve represents the defect synthetic beam signal obtained by the proposed curved lead-seal imaging algorithm. The red curve has a higher amplitude than the black curve, indicating that the proposed algorithm improves the coherent summation of defect echoes after delay correction. Therefore, the curved lead-seal imaging algorithm can enhance the defect echo signal and improve the imaging quality of curved lead-seal defects.

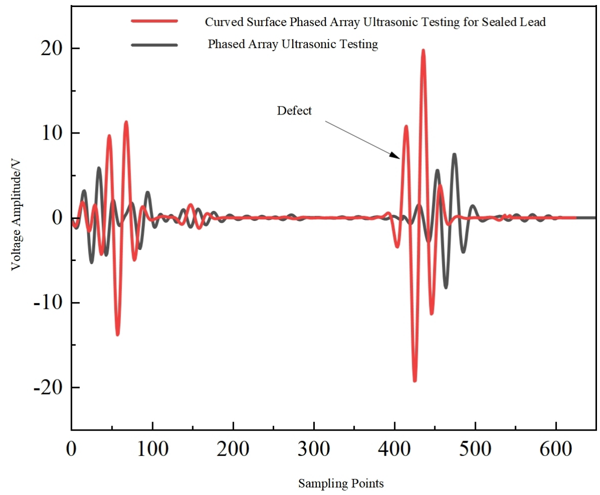


**Figure 16.** Defect echo synthetic beam signal for lead seals.

Overall, the results shown in **Figures 8–16** demonstrate that the proposed curvature-adaptive imaging algorithm can convert the calculated delay into sampling-point compensation, enhance defect echo signals through delay-and-sum processing, extract a smoother envelope representation through Hilbert transform, and reduce geometric distortion through angular coordinate correction. Compared with conventional phased-array imaging, the proposed method provides clearer defect indication, higher synthetic echo amplitude, and lower positioning error for curved lead-seal defect imaging.

## 5. Experimental validation on lead-seal specimens with different artificial defects

To further verify the effectiveness of the proposed curvature-adaptive imaging algorithm, ultrasonic phased-array experiments were carried out on lead-seal specimens with artificial defects. The purpose of the experiment was to evaluate whether the proposed method can improve defect localization accuracy, defect-shape consistency, and imaging quality under practical testing conditions. The same experimental echo data were processed by both the conventional phased-array imaging algorithm and the proposed curvature-adaptive imaging algorithm, and the corresponding imaging results were compared.

### 5.1. Experimental specimens and testing system

A high-voltage cable termination is mainly composed of the tail pipe, aluminum sheath, lead seal, and other structural components. The lead seal is an important sealing and connecting structure in the cable termination. Defects in the lead seal may affect the sealing performance and long-term operational reliability of the cable termination. The actual lead-seal structure of the cable termination is shown in **Figure 17a**, and the schematic diagram of the defect locations is shown in **Figure 17b**.

**(a)** Actual lead seal of the cable termination.

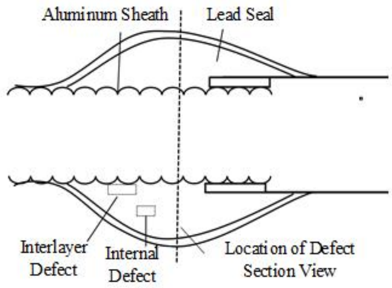


**(b)** Schematic diagram of lead-seal defect locations.

**Figure 17.** Actual lead-seal structure and schematic diagram of defect locations.

According to the actual distribution characteristics of lead-seal defects, the defects located closer to the upper surface of the lead seal were regarded as internal lead-seal defects, while the defects located closer to the aluminum sheath were regarded as interlayer lead-seal defects. Artificial lead-seal defects were used in the experiment because their defect characteristics are similar to those of naturally formed lead-seal defects. In addition, artificial defects can effectively shorten the specimen preparation period, reduce experimental cost, and ensure controllable defect size and location.

Several circular-hole defects were fabricated in the lead-seal specimens. The internal circular-hole defects were set at centre depths of 10 mm, 13 mm, 15 mm, and 18 mm from the upper surface of the lead seal. In addition, an interlayer circular-hole defect was set at a centre depth of 25 mm from the upper surface of the lead seal. In the experimental verification, two representative defects were mainly selected: an internal circular-hole defect with a centre depth of 15 mm and a diameter of 3 mm, and an interlayer circular-hole defect with a centre depth of 25 mm and a diameter of 3 mm. These defects were used to evaluate the imaging performance of the proposed method for both internal defects and interlayer defects.

The ultrasonic phased-array testing system used in this experiment consisted of a phased-array ultrasonic instrument, a one-dimensional linear-array probe, liquid couplant, lead-seal defect specimens, and a display and data-processing system. The ultrasonic phased-array instrument was a CTS-PA22X phased-array detector provided by Guangdong Shantou Ultrasonic Electronics Co., Ltd. The one-dimensional linear-array probe had a centre frequency of 2 MHz, 16 elements, an element pitch of 0.5 mm, and an element length of 10 mm.

The main technical parameters of the ultrasonic phased-array testing system are listed in **Table 2**.

**Table 2.** Technical parameters of the ultrasonic phased-array testing system.

| Parameter | Setting |
| --- | --- |
| Instrument model | CTS-PA22X |
| Wave mode | Longitudinal wave |
| Sound velocity | 2,300 m/s |
| Excitation voltage | 95 V |
| Pulse repetition frequency | 1,000 Hz |
| Scanning type | Sector scan |
| Focusing type | Equal sound-path focusing |

**Table 2.** *Cont.*

| Parameter | Setting |
|---|---|
| Start angle / stop angle | −30°–30° |
| Digital gain | 20 dB |
| Analog gain | 35 dB |
| Filter bandwidth | 0.5–10 MHz, adjustable |
| Probe frequency | 2 MHz |
| Number of probe elements | 16 |
| Element pitch | 0.5 mm |
| Element length | 10 mm |

The experimental platform for ultrasonic imaging of curved lead-seal defects is shown in **Figure 18**.

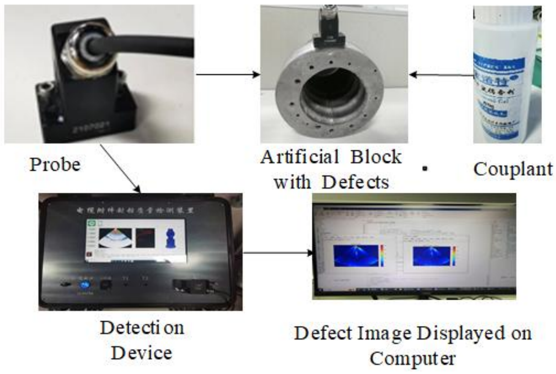


**Figure 18.** Experimental platform for ultrasonic imaging of curved lead-seal defects.

During the experiment, the phased-array probe was placed on the curved lead-seal surface with liquid couplant applied between the probe and the specimen. The ultrasonic wave emitted by the probe propagated through the couplant into the lead-seal specimen. When the acoustic wave encountered a defect, part of the acoustic energy was reflected and received by the phased-array elements. The received echo signals were collected by the ultrasonic phased-array instrument and then exported for data processing. Finally, MATLAB was used to process the defect echo data by the conventional phased-array imaging algorithm and the proposed curvature-adaptive imaging algorithm. The imaging results obtained by the two methods were then compared.

## 5.2. Experimental specimens and testing system

The internal lead-seal defect was first tested using the experimental platform described above. The sector-scan angle was set from −30° to 30°, and the focusing depth was set to 15 mm. After acquiring the ultrasonic phased-array echo data, the conventional phased-array imaging algorithm and the proposed curvature-adaptive imaging algorithm were used to reconstruct the defect image. The imaging results are shown in **Figure 19**.

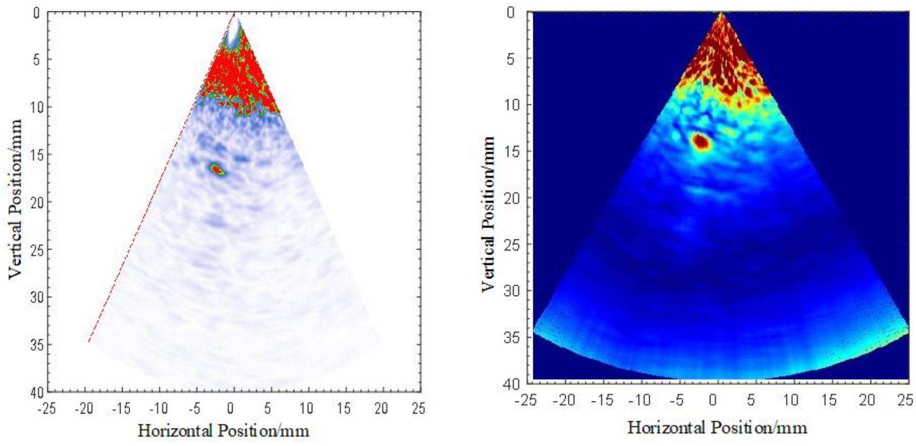


**(a)** Conventional phased-array imaging. **(b)** Curvature-adaptive lead-seal imaging.

**Figure 19.** Ultrasonic imaging results of the internal lead-seal defect.

In the imaging results, the image data were displayed by color mapping. A larger synthesized defect-echo amplitude corresponds to a larger pixel value and a higher image intensity. The image intensity increases from blue to green and then to red. The red region near the upper part of the image corresponds to the near-surface blind zone. This region is caused by repeated reflections of ultrasonic waves near the lead-seal surface. The acoustic field in this region is complex and has high amplitude, which may mask defect echoes close to the surface.

As shown in **Figure 19a**, when the conventional phased-array imaging algorithm is used, the reconstructed internal defect presents an elliptical shape, and the defect morphology deviates from the actual circular-hole feature. The detected defect depth range is 16–18 mm. Therefore, the measured centre depth is taken as the midpoint of this range, namely 17.0 mm. Since the actual centre depth of the internal defect is 15.0 mm, the positioning error of the conventional phased-array imaging algorithm is 13.33%.

As shown in **Figure 19b**, when the proposed curvature-adaptive imaging algorithm is used, the reconstructed internal defect is closer to a circular shape. The detected defect depth range is 13–15 mm, and the measured centre depth is 14.0 mm. Compared with the actual defect depth of 15.0 mm, the positioning error is 6.67%. This result indicates that the proposed curvature-adaptive imaging algorithm can reduce the localization deviation caused by the curved lead-seal surface. In addition, the reconstructed defect morphology is more consistent with the actual circular-hole defect.

Compared with conventional phased-array imaging, the proposed method provides a clearer defect indication and a defect shape closer to the real circular-hole morphology. This improvement is mainly attributed to the curvature-adaptive delay compensation. By considering the acoustic propagation path through the curved couplant–lead interface, the proposed method can reduce the phase mismatch among array-element echoes and improve the focusing accuracy of the defect image.

### 5.3. Imaging results of the interlayer lead-seal defect

To evaluate the applicability of the proposed method to interlayer defects, the interlayer circular-hole defect with a centre depth of 25.0 mm and a diameter of 3 mm was tested. The same 2 MHz phased-array probe was used, the sector-scan angle was set from −30° to 30°, and the focusing depth was set to 15 mm. The imaging results obtained by the two algorithms are shown in **Figure 20**.

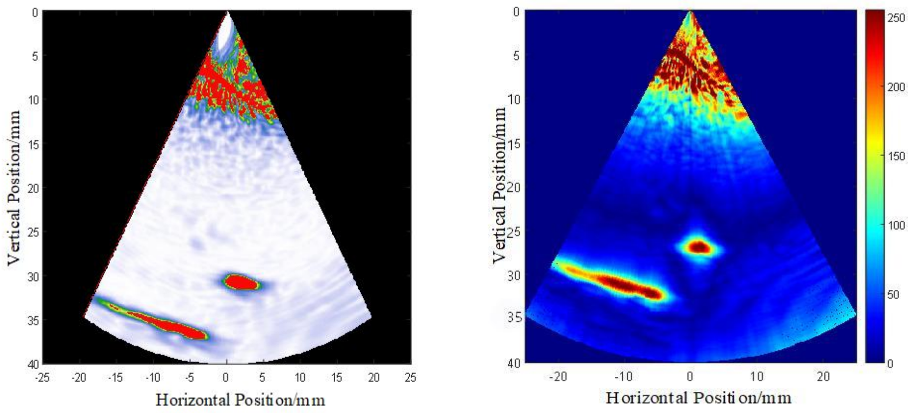


**(a)** Conventional phased-array imaging. **(b)** Curvature-adaptive lead-seal imaging.

**Figure 20.** Ultrasonic imaging results of the interlayer lead-seal defect.

Since the interlayer defect is close to the aluminum sheath, a bottom echo appears below the defect indication. As shown in **Figure 20a**, when the conventional phased-array imaging algorithm is used, the interlayer defect is reconstructed within the depth range of 27–28 mm. The measured centre depth is therefore 27.5 mm. Compared with the actual defect depth of 25.0 mm, the positioning error is 10.00%. In addition, the reconstructed defect shape is close to an ellipse, although the defect centre still shows a high pixel value and the surrounding noise is weak.

As shown in **Figure 20b**, when the proposed curvature-adaptive imaging algorithm is used, the interlayer defect is reconstructed within the depth range of 25–27 mm. The measured centre depth is 26.0 mm, and the positioning error is 4.00%. The reconstructed defect shape is closer to a circular feature, and the defect centre also presents a high pixel value. The surrounding noise remains low.

Compared with the conventional phased-array imaging result, the proposed curvature-adaptive imaging algorithm reduces the positioning error of the interlayer defect from 10.00% to 4.00%. This result indicates that the proposed method is not only effective for internal defects, but also applicable to interlayer defects near the aluminum sheath. Although the noise level in the two images is relatively low, the proposed method provides a more accurate defect position and a defect morphology closer to the actual circular-hole defect.

### 5.4. Imaging results of combined internal and interlayer defects

To further evaluate the performance of the proposed method under more complex defect conditions, a lead-seal specimen containing both an internal defect and an interlayer defect was tested. The internal defect had an actual centre depth of 15.0 mm, and the interlayer defect had an actual centre depth of 25.0 mm. The same experimental parameters were used. The imaging results are shown in **Figure 21**.

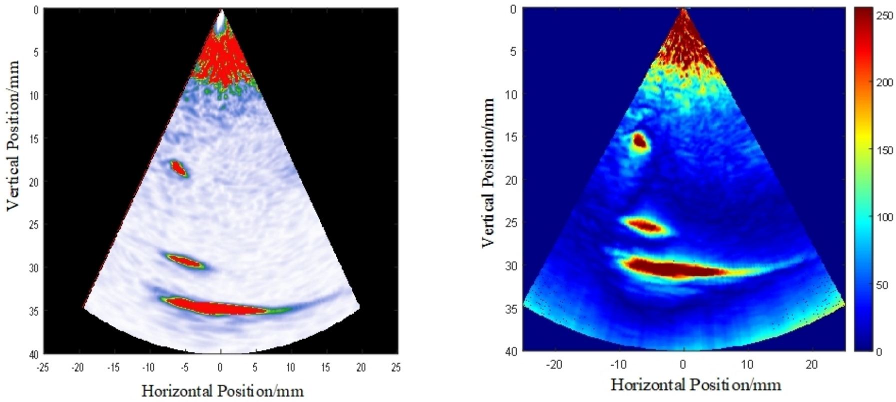


**(a)** Conventional phased-array imaging. **(b)** Curvature-adaptive lead-seal imaging.

**Figure 21.** Ultrasonic imaging results of combined internal and interlayer lead-seal defects.

As shown in **Figure 21a**, when the conventional phased-array imaging algorithm is used, the internal defect is reconstructed within the depth range of 15–16 mm, and the measured centre depth is 15.5 mm. Therefore, the positioning error of the internal defect is 3.33%. The interlayer defect is reconstructed within the depth range of 27–28 mm, and the measured centre depth is 27.5 mm. Compared with the actual interlayer defect depth of 25.0 mm, the positioning error is 10.00%. Although both defects can be identified by the conventional phased-array imaging algorithm, the interlayer defect shows an obvious depth deviation.

As shown in **Figure 21b**, when the proposed curvature-adaptive imaging algorithm is used, the internal defect is also reconstructed within the depth range of 15–16 mm, and the measured centre depth is 15.5 mm. The corresponding positioning error is 3.33%, which is the same as that obtained by the conventional phased-array imaging algorithm. However, the interlayer defect is reconstructed within the depth range of 25–27 mm, and the measured centre depth is 26.0 mm. The positioning error of the interlayer defect is reduced to 4.00%.

The comparison shows that both algorithms can locate the internal defect in the combined-defect specimen with similar accuracy. However, for the deeper interlayer defect, the proposed curvature-adaptive imaging algorithm provides a more accurate localization result. This indicates that the proposed method is particularly effective in correcting the depth deviation of interlayer defects caused by curved-surface propagation.

It should also be noted that the internal defect in **Figure 21b** is consistent with the internal defect imaging result shown in **Figure 19b**, while the interlayer defect differs to some extent from the result shown in **Figure 20b**. This is mainly because the focusing depth was set to 15 mm in the experiment. The focusing depth is close to the internal defect but relatively far from the interlayer defect at 25 mm. As a result, the synthesized echo amplitude of the interlayer defect is lower than that of the internal defect. This phenomenon indicates that the focusing depth has an important influence on the imaging quality of defects at different depths. Therefore, the optimization of phased-array testing parameters should be further considered for curved lead-seal imaging.

### 5.5. Quantitative comparison and discussion

To quantitatively compare the localization performance of the conventional phased-array imaging algorithm and the proposed curvature-adaptive imaging algorithm, the measured centre depth of each defect was determined using the midpoint of the detected depth range. The positioning error was calculated as

$$\varepsilon = \frac{|d_m - d_0|}{d_0} \times 100\% \tag{25}$$

As shown in **Table 3**, for the single internal defect, the positioning error is reduced from 13.33% to 6.67% after applying the proposed curvature-adaptive imaging algorithm. For the single interlayer defect, the positioning error is reduced from 10.00% to 4.00%. In the combined-defect specimen, both algorithms locate the internal defect with a positioning error of 3.33%. However, for the interlayer defect in the same specimen, the proposed method reduces the positioning error from 10.00% to 4.00%.

**Table 3.** Quantitative comparison of defect localization results obtained by different imaging algorithms.

| Defect type | Actual depth/mm | Imaging algorithm | Detected depth range/mm | Measured centre depth/mm | Positioning error/% |
|---|---|---|---|---|---|
| Internal defect | 15.0 | Conventional phased-array imaging | 16–18 | 17.0 | 13.33 |
| Internal defect | 15.0 | Proposed curvature-adaptive imaging | 13–15 | 14.0 | 6.67 |
| Interlayer defect | 25.0 | Conventional phased-array imaging | 27–28 | 27.5 | 10.00 |
| Interlayer defect | 25.0 | Proposed curvature-adaptive imaging | 25–27 | 26.0 | 4.00 |
| Combined defect—internal defect | 15.0 | Conventional phased-array imaging | 15–16 | 15.5 | 3.33 |
| Combined defect—internal defect | 15.0 | Proposed curvature-adaptive imaging | 15–16 | 15.5 | 3.33 |
| Combined defect—interlayer defect | 25.0 | Conventional phased-array imaging | 27–28 | 27.5 | 10.00 |
| Combined defect—interlayer defect | 25.0 | Proposed curvature-adaptive imaging | 25–27 | 26.0 | 4.00 |

These results demonstrate that the proposed curvature-adaptive imaging algorithm improves defect localization accuracy, especially for defects located near the aluminum sheath. The improvement mainly comes from the curvature-adaptive delay compensation. In conventional phased-array imaging, the curved lead-seal surface is usually simplified as a planar interface, which causes propagation-time errors and phase mismatch among the echo signals received by different array elements. In the proposed method, the propagation path through the curved couplant–lead interface is considered, and the calculated delay is used to align the echo signals before coherent summation. Therefore, the defect echo can be more effectively focused, and the reconstructed defect position is closer to the actual defect location.

Overall, the experimental results verify that the proposed curvature-adaptive imaging algorithm can effectively improve the ultrasonic imaging quality of curved lead-seal defects. Compared with conventional phased-array imaging, the proposed method produces clearer defect indications, better defect-shape consistency, and lower positioning error. The method is applicable to internal defects, interlayer defects, and combined internal–interlayer defects in curved lead-seal structures.

## 6. Conclusions

In this study, a curvature-adaptive ultrasonic phased-array imaging method was proposed for defect detection in curved lead-seal structures of high-voltage cable terminations. Based on Fermat's principle and Snell's law, the propagation path through the curved couplant–lead interface was analyzed, and the corresponding delay compensation method was established. Numerical simulation results showed that the curved lead-seal surface caused beam spreading and focal-position shift compared with the flat-interface case, indicating that conventional planar-interface delay laws may lead to localization errors in curved lead-seal imaging.

Based on the curved-interface delay calculation, a curvature-adaptive delay-and-sum imaging algorithm was implemented. The calculated delay times were converted into sampling-point compensation values to align the echo signals received by different array elements before coherent summation. Hilbert envelope extraction and angular coordinate correction were then used to improve image display and spatial localization. Compared with conventional phased-array imaging, the proposed method produced clearer defect indications and reduced geometric distortion in the reconstructed images.

Experimental results on lead-seal specimens further verified the effectiveness of the proposed method. For the internal defect with an actual depth of 15.0 mm, the positioning error was reduced from 13.33% to 6.67%. For the interlayer defect with an actual depth of 25.0 mm, the positioning error was reduced from 10.00% to 4.00%. In the combined-defect specimen, the proposed method also improved the localization accuracy of the interlayer defect. These results demonstrate that the proposed curvature-adaptive imaging method can effectively improve defect localization accuracy and imaging quality for curved lead-seal structures. Future work will focus on naturally formed defects, irregular crack-like defects, variable couplant conditions, and field testing applications.

**Author contributions:** Conceptualization, JC; methodology, LH; software, LH and LW; validation, FZ and QZ; formal analysis, LW; investigation, FZ and QZ; resources, LW; data curation, LW; writing—original draft preparation, JC; writing—review and editing, JC; visualization, FZ; supervision, JC; project administration, JC; funding acquisition, JC. All authors have read and agreed to the published version of the manuscript.

**Funding:** This research was supported by the Science and Technology Project of Shenzhen Power Supply Co., Ltd. under Grant No. 090000KC24010007 (Project Name: Research on Technology and Device for Defect Detection of Lead Sealing and Oil Leakage in High-Voltage Cable Accessories).

**Institutional review board statement:** Not applicable.

**Informed consent statement:** Not applicable.

**Data availability statement:** The data used in this study are available from the corresponding author upon reasonable request.

**Conflict of interest:** The authors declare no conflict of interest.

**AI use statement:** The authors declare that no artificial intelligence (AI) tools were used in the preparation of this manuscript.

## References

1. Xu ZL, Feng Y, Yang YP, et al. Diagnosis of electrochemical corrosion and water ingress defects in lead seal section of high-voltage cable intermediate joints. Insulating Materials. 2022; 55(11): 118–126. (in Chinese)
2. Fang CH, Hu DS, Tao YN, et al. Flexible coupling inspection of lead seal defects in high-voltage cable terminals using phased array ultrasonic testing. High Voltage Engineering. 2022; 48(1): 29–37. (in Chinese)
3. Fang CH, Hu DS, Guo KG, et al. Research on ultrasonic testing method for lead seal defects in high-voltage cable terminals. China Measurement & Test. 2022; 48(3): 118–123. (in Chinese)
4. Drinkwater BW, Wilcox PD. Ultrasonic arrays for non-destructive evaluation: A review. NDT & E International. 2006; 39(7): 525–541. doi: 10.1016/j.ndteint.2006.03.006
5. Holmes C, Drinkwater BW, Wilcox PD. Post-processing of the full matrix of ultrasonic transmit-receive array data for non-destructive evaluation. NDT & E International. 2005; 38(8): 701–711. doi: 10.1016/j.ndteint.2005.04.002
6. Zhang J, Drinkwater BW, Wilcox PD, et al. Defect detection using ultrasonic arrays: The multi-mode total focusing method. NDT & E International. 2010; 43(2): 123–133. doi: 10.1016/j.ndteint.2009.10.001
7. Li W, Zhou Z, Li Y. Inspection of butt welds for complex surface parts using ultrasonic phased array. Ultrasonics. 2019; 96: 75–82. doi: 10.1016/j.ultras.2019.02.011
8. Cruza JF, Camacho J, Moreno JM, et al. Ultrafast hardware-based focal law calculator for automatic focusing. NDT & E International. 2015; 74: 1–7. doi: 10.1016/j.ndteint.2015.04.003
9. Miao W, Liu N, Huang J, et al. Adaptive ultrasonic full matrix capture process for the global imaging of complex components with curved surfaces. Sensors. 2024; 24(1): 225. doi: 10.3390/s24010225
10. Wang J, Zhou Z, Li Y, et al. A high efficiency adaptive ultrasonic array imaging method with sensitivity correction for curved structures. Measurement. 2024; 238: 115322. doi: 10.1016/j.measurement.2024.115322
11. Chatillon S, Cattiaux G, Serre M, et al. Ultrasonic non-destructive testing of pieces of complex geometry with a flexible phased array transducer. Ultrasonics. 2000; 38(1–8): 131–134.
12. Casula O, Poidevin C, Cattiaux G, et al. Control of complex components with smart flexible phased arrays. AIP Conference Proceedings. 2006; 820(1): 829–836.
13. Guan S, Wang X, Hua L, et al. Ultrasonic phased array inspection of aeroengine casing ring forgings using adaptive filtering and angle gain compensation algorithm. Applied Acoustics. 2022; 195: 108833.
14. Peng ZP, Zheng JS, Zhen ZM, et al. Ultrasonic phased array flexible coupling detection of defects in high-voltage cable terminal lead seals. Frontiers in Mechanical Engineering. 2025; 11: 1467079. doi: 10.3389/fmech.2025.1467079
15. Zheng H, Cai QS, Zheng JS, et al. Quantitative method for ultrasonic testing of lead seal defects in high voltage cable accessories. IEEE Access. 2025; 13: 76047–76057. doi: 10.1109/ACCESS.2025.3565290
16. Fang CH, Gao SQ, Xia R, et al. Three-dimensional imaging detection of lead seal defects in high-voltage cable terminations using a one-D phased array. Technical Acoustics. 2026; 46: 1–11. doi: 10.16300/j.cnki.1000-3630.25091101 (in Chinese)
17. Zhou LG, Li WH, Lu X, et al. Ultrasonic image recognition of terminal lead seal defects based on convolutional neural network. In: Dong X, Cai L (editors). The Proceedings of 2023 4th International Symposium on Insulation and Discharge Computation for Power Equipment. Lecture Notes in Electrical Engineering. Springer; 2024. 1100, pp. 77–88. doi: 10.1007/978-981-99-7393-4_8
18. Tunukovic V, McKnight S, Mohseni E, et al. A study of machine learning object detection performance for phased array ultrasonic testing of carbon fibre reinforced plastics. NDT & E International. 2024; 144: 103094. doi: 10.1016/j.ndteint.2024.103094
19. Na Y, He Y, Deng B, et al. Advances of machine learning in phased array ultrasonic non-destructive testing: A review. AI. 2025; 6(6): 124. doi: 10.3390/ai6060124
20. Ma M, Wang Z, Gao Z, et al. Ultrasonic phased array testing and identification of multiple-type internal defects in carbon fiber reinforced plastics based on convolutional neural network. Materials. 2025; 18(2): 318. doi:

10.3390/ma18020318
21. Nicolson E, Mohseni E, Lines D, et al. Towards an in-process ultrasonic phased array inspection method for narrow-gap welds. NDT & E International. 2024; 144: 103074. doi: 10.1016/j.ndteint.2024.103074
22. Chen XQ, Gong SF, Pan W, et al. Study on denoising method of weld defect signal based on SSA-VMD-WPD. Applied Sciences. 2024; 14(16): 7251. doi: 10.3390/app14167251
23. Deng B, Wu ZL, Yan R, et al. Study on ultrasonic phased array inspection method of crack defects in butt joints of multi-layered steel vessel for high-pressure hydrogen storage. Energies. 2025; 18(20): 5419. doi: 10.3390/en18205419
24. Pan NK, Shao B, Fang CH. Research of total-focusing-imaging based on phase coherence and dB amplitude enhancement. AIP Advances. 2025; 15(3): 035245.
25. Zhu J, Wang G, Luo K, et al. Ultrasonic nondestructive testing image enhancement based on deep learning. Applied Sciences. 2025; 15(15): 8339.